

PAPER

Stability threshold of formamidinium lead iodide determined by strain amplitudes

To cite this article: S Karthick *et al* 2020 *J. Phys. D: Appl. Phys.* **53** 504003

View the [article online](#) for updates and enhancements.



IOP | ebooks™

Bringing together innovative digital publishing with leading authors from the global scientific community.

Start exploring the collection—download the first chapter of every title for free.

Stability threshold of formamidinium lead iodide determined by strain amplitudes

S Karthick¹ , J J Ríos-Ramírez² , S Velumani^{2,5} , K S Martirosyan³ 
and H Castaneda⁴ 

¹ Programa de Nanociencias y Nanotecnología, Centro de Investigación y de Estudios Avanzados del Instituto Politécnico Nacional (CINVESTAV-IPN), Av. Instituto Politécnico Nacional 2508, Col. San Pedro Zacatenco, Ciudad de México Código Postal 07360, Mexico

² Departamento de Ingeniería Eléctrica (SEES), Centro de Investigación y de Estudios Avanzados del Instituto Politécnico Nacional (CINVESTAV-IPN), Av. Instituto Politécnico Nacional 2508, Col. San Pedro Zacatenco, Ciudad de México Código Postal 07360, Mexico

³ Department of Physics and Astronomy, University of Texas Rio Grande Valley, Brownsville TX 78520, United States of America

⁴ Department of Materials Science and Engineering, National Corrosion and Materials Reliability Center, Texas A & M University, Texas, United States of America

E-mail: velu@cinvestav.mx

Received 26 April 2020, revised 23 August 2020

Accepted for publication 3 September 2020

Published 8 October 2020



CrossMark

Abstract

The mechanical stability of α -phase formamidinium (FA) lead iodide perovskite is investigated using a systematic finite deformation method based on all the possible FA cation orientations, inside an inorganic cage. Two specific strain boundaries of deformation or strain amplitudes were efficiently examined over this optimized pseudo-cubic structure, which needs nine independent elastic constants (EC) to determine the stability. The stable structure was found while applying an initial amplitude limit (0.02), which is attributed to the balanced charge distribution in between the hydrogens (H_4 , H_5 and H_2 , H_3) to the specific iodine (I_2) atom. Surprisingly, with increasing amplitude (0.04), the structure was unstable due to their disturbed charge distribution and FA cation tilting as found from electron density difference (EDD) spectrum. From the computational perspective, the obtained EC values, Mulliken charge, and EDD results provide some crucial information's to understand the reason behind the instability issues based on the FA cation position which is reported so far. Hence, we provide a solid justification regarding the stability threshold of a pseudo-cubic model based on the FA cation position to get an insight into this FA cation-based perovskite material.

Keywords: formamidinium-lead-iodide-perovskite, density-functional-theory, van der Waals, elastic constant, stability

(Some figures may appear in colour only in the online journal)

1. Introduction

The general representation of an Organo-lead Halide based Perovskite Solar Cell (OIHPSC) is of the form ABX_3 , where A

is the organic or inorganic cations such as methylammonium CH_3NH_3 (MA^+), formamidinium $HC(NH_2)_2$ (FA^+), cesium (Cs^+), or rubidium (Rb^+), meanwhile, B represents the larger metal cations like lead (Pb), or tin (Sn), with X as the smaller halogen anions, generally bromide (Br^-), chloride (Cl^-) or iodide (I^-). The $FAPbI_3$ perovskites show a broader absorption range [1, 2], larger organic cation radii [3], long diffusion

⁵ Author to whom any correspondence should be addressed

length [4], low exciton binding energy [5], higher thermal stability [6] and longer phonon relaxation lifetime [7] and a smaller optical band gap [8], compared with MA and Cs based perovskites, making it as a favorable candidate for its application as an absorber layer in solar cells. Constantinou C. Stoumpos *et al* [1] discussed the phase transition of FAPbI₃ perovskites and they generally classified the phases based on the transition temperatures: α -phase ($T \sim 293$ K), β -phase ($T \sim 150$ K), γ -phase ($T \sim 100$ K) and a degraded δ -phase, referred as non-perovskite yellow phase. At room temperature α -phase (black phase) and β -phase of FAPbI₃, adopt the space group P₃m1 and P3, respectively. On the other hand, the non-perovskite δ -phase shows a hexagonal P6₃mc phase, which is not suitable for photovoltaic applications. Therefore, the structural stability from the α -phase of the FAPbI₃ perovskite has turned into an active research topic.

A. A. Zhumekenov *et al* [4] synthesized both FAPbI₃ & FAPbBr₃ single crystals by the inverse temperature crystallization method (ITC). The authors obtained cubic structures for both cases with a space group Pm-3m and lattice parameters equal to: $a = 5.940$ Å for FAPbBr₃ and $a = 6.357$ Å for FAPbI₃. The degradation was tested both at room temperature and at 185 °C for 1 h, and the annealed samples had long-term stability (~ 7 d) compared to the former case (~ 7 h). Also, the authors showed that a lower carrier mobility might be related to the instability of the FAPbI₃ perovskites. Recent investigation demonstrated that the materials, architecture, and structure of the perovskite interface might play a crucial role in both degradation rates and durability of the photovoltaic device [9]. A. C. Ferreira *et al* [10] investigated the cubic α - FAPbI₃ single-crystal by coherent inelastic neutron scattering spectroscopy (INS), Brillouin light scattering (BLS), and low frequency acoustic phonon measurements, the authors provide the complete set of elastic constant values (EC) at room temperature, mentioning that both the structural stability and the ultra-low thermal conductivity are related to the softness of the FA and MA cations. A negative value in c_{12} is obtained, explaining that in its uniaxial compression along [100], compared to [010] and [001], the structure tries to maintain an anisotropic behavior. Such a value generates a low bulk modulus with the fulfillment of the stability criteria. The authors mainly noticed that the structural instability occurred when the lattice parameters exceed 6.4 Å, decreasing both c_{11} and the bulk modulus magnitudes. Based on their results, they concluded that iodide-based materials have the lowest elastic stiffness compared to bromide-based materials.

First principle calculations by J. F. Wang *et al* studied the electrical and optical properties of the FAPbI₃ perovskite structure, by means of a DFT + vdW [11] scheme. The authors found a lattice parameter equal to $a = 6.353$ Å, with hydrogen bonds in between the NH₂ group and the I atom, as well as the hybridization among Pb (s) - I (p) in the Valence Band Maximum (VBM) as a prominent features for the stability of the FAPbI₃ structure. On the other hand, the three EC of the cubic FAPbI₃ (c_{11} , c_{12} , c_{44}) fulfill the stability conditions [12]. With respect to the organic cation rotation, M.A. Carignano *et al* investigated FAPbI₃ by means of first-principles molecular dynamics along with group theory, finding that the rotation

along the N-N axis of the FA cation is anisotropic at room temperature, and a ΔT activates the C-N bond axis mode, concluding that the instability of the FAPbI₃ structure is related with the three M⁺ modes in collaboration with a rotation of the PBI₆ octahedra and with the effect of the reorientation of the organic FA cation [13]. Meanwhile, S. Kanno *et al* theoretically analyzed the energy barriers as well as the potential energy surfaces obtained by the rotation of the organic FA cation inside the cubic cage, finding that the FA cation freely rotates around the N-N bond axis (φ) as compared to the least favorable one defined by the sum of the two vectors of the C-N bond axis (θ). Based in a vdW-DF2 [14] method, the authors calculated a compressed set of FAPbI₃ lattice parameters ($a = 6.50$ Å, $b = 6.48$ Å and $c = 6.53$ Å) compared the one determined by a plane DFT method ($a = 6.58$ Å, $b = 6.59$ Å and $c = 6.60$ Å), obtaining a pseudo-cubic structures for both cases. The author reported that the rotational barrier heights (RBH) for both angles (φ & θ) follows the halogen-based order as: I < Br < Cl, concluding that the halogen substitution significantly influences the θ RBH alone, consolidating a way to control the rotation of the FA cation [15].

In this work, the mechanical stability from the pseudo-cubic unit cell of the pristine formamidinium lead iodide perovskite was systematically investigated and presented, by means of a finite deformation method solved by density functional theory calculations. It is shown for the first time, that the stability conditions from this orthorhombic model were fulfilled uniquely whether the boundary of deformation, known as strain amplitude, was kept below 0.02 for the nine strain tensors. Furthermore, it is evidently identified a direct correlation in the elastic response of the material with respect to the main charge distribution, found in between the cation terminations and the halogens lattice, a fact that is thoroughly validated in a set of 12 FA cation orientations provided by its space group. The mechanical instability is finally found for a strain amplitude equal to 0.04. Specifically, for two-dimensional deformations that alter the interactions among the hydrogen-nitrogen terminations and the iodine positions. In addition to this prominent result, it was seen that the atomic relaxation, at this level of strain, collectively drives the whole organic cation outside its initial position into a tilted orientation that follows a charge rearrangement. The present contribution provides novel descriptions aiming to tackle the instability related with the degradation process from the alpha perovskite phase. This is the first report, which is evidently explains the instability issue of pristine formamidinium lead iodide perovskites based on their elastic constant results correlated with their electron density difference and Mulliken charge values (both bond population and bond length), to our knowledge, such systematic analysis have not been reported before.

2. Structural analysis of FAPbI₃ perovskite

Our previous work [16] on the structural analysis of FAPbI₃ perovskite showed the equilibrium lattice parameters follow two tendencies, as a function of the clockwise rotation of the FA cation. For the first case, the length of the lattice parameter

that is parallel to the N–N axis is larger and the one perpendicular diminishes its length, becoming the most compact. This geometrical relaxation occurred only to the lattice parameters extended along the FA cation plane. For the second case, the direction that is perpendicular to the planar cation does not show any variations during the cell optimization, consolidating a uniform behavior. Despite these results, both b/a and c/a ratios acquire close values with respect to the cubic symmetry ($\frac{b}{a} = 0.973$, $\frac{c}{a} = 0.991$), in agreement with early cited pseudo-cubic results [15]. The strongest modification in the inorganic sub-cell was observed in the iodine positions, measured with the aid of the Pb–I–Pb angle, in which the iodine tends to reduce the distance to the N–H terminations at the ground state. Finally, the Electron Difference Density (EDD) exhibits a stronger electronic density distribution among the H₄ and H₅ hydrogen and the I₂ atoms (see figure 1), meanwhile, a weaker distribution of charge is found in between the lead atoms and the FA cation. Hence in the present work, we report the evaluation of the structural stability from the pseudo-cubic FAPbI₃ perovskites, as generated by the $Pm-3m$ space group, by means of the EC $\{c_{ij}\}$ set calculation. The results show that a specific strain above a critical deformation could turn the structure unstable followed by a FA cation tilting along with disproportionation of bonds, hence, defining a possible structural indicator to track the stability of pure FAPbI₃.

3. Computational details

3.1. Self-consistent cycle methodology

The calculations were performed by means of a DFT-vdW scheme, by the Tkatchenko-Scheffler dispersion model [11], through the CASTEP [17] module available in the Material studio package [18]. For all calculations, the GGA–PBE exchange-correlation function [19] was considered, with ultra-soft pseudopotentials [20]. A k -point mesh of $4 \times 4 \times 4$ for all the conventional unit cell models (32 points and a 0.035 grid separation) along with a plane wave cutoff energy of 400 eV were chosen by carefully testing the convergence under the BFGS algorithm [21]. As in our previous contribution, the structures were generated by the rotation of the organic FA cation inside the inorganic cage, orienting the FA molecule in a clockwise direction using the C–H₁ bond as the hour hand of a clock, namely 12:00, 03:00, 06:00, and 09:00 hrs. positions, with the carbon atom pointing outwards at each angular position. The 12 possibilities are generated for the three crystalline planes [(100) 12:00 to 09:00, (010) 12:00 to 09:00 and (001) 12:00 to 09:00], as it is represented by the space group $Pm-3m$, from which both initial lattice parameters and atomic positions were also taken [22]. For the full EC calculation, a finer scheme was chosen with an energy, force and displacement convergence criteria equal to 4×10^{-6} eV atom⁻¹, 0.01 eV Å⁻¹ and 4×10^{-4} Å, respectively.

3.2. c_{ij} calculation method

The present finite deformation method was defined by two strain amplitudes ($\delta_{\max} = 0.02$ and $\delta_{\max} = 0.04$), that

establish different deformation boundaries within six strain steps $\{\delta_i = \pm 0.004, \pm 0.012$ and $\pm 0.020\}$ and $\{\delta_i = \pm 0.008, \pm 0.024$ and $\pm 0.040\}$, for each deformation boundaries respectively, in agreement with recommended deformation boundaries [23], with both parameters carefully tested against the point dispersion of the strain energy difference (ΔE_i).

The strained structures are generated by means of a transformation of the optimized set of lattice parameters [23] given as:

$$\begin{Bmatrix} x' \\ y' \\ z' \end{Bmatrix} = (D(e) + I) \begin{Bmatrix} x \\ y \\ z \end{Bmatrix} \quad (1)$$

where $\begin{Bmatrix} x' \\ y' \\ z' \end{Bmatrix}$ is the new set of strained vectors and $\begin{Bmatrix} x \\ y \\ z \end{Bmatrix}$ corresponds to any ground state lattice vector to be modified by the strained tensor $(D(e) + I)$. For an orthorhombic structure, nine independent strain patterns are needed to determine the adiabatic EC values. The first three of them act along a single direction (D_1, D_2, D_3), meanwhile, the remaining six modify an entire crystalline plane, i.e. the deformation acts along with two directions ($D_4, D_5, D_6, D_7, D_8, D_9$), both set of strain patterns are written as [24, 25]:

$$D_1 = \begin{Bmatrix} (1 + \delta) & 0 & 0 \\ 0 & 1 & 0 \\ 0 & 0 & 1 \end{Bmatrix}, \quad (2)$$

$$D_2 = \begin{Bmatrix} 1 & 0 & 0 \\ 0 & (1 + \delta) & 0 \\ 0 & 0 & 1 \end{Bmatrix}, \quad (3)$$

$$D_3 = \begin{Bmatrix} 1 & 0 & 0 \\ 0 & 1 & 0 \\ 0 & 0 & (1 + \delta) \end{Bmatrix}, \quad (4)$$

$$D_4 = \begin{Bmatrix} u & 0 & 0 \\ 0 & u & \delta u \\ 0 & \delta u & u \end{Bmatrix}, \quad (5)$$

$$D_5 = \begin{Bmatrix} u & 0 & \delta u \\ 0 & u & 0 \\ \delta u & 0 & u \end{Bmatrix}, \quad (6)$$

$$D_6 = \begin{Bmatrix} u & \delta u & 0 \\ \delta u & u & 0 \\ 0 & 0 & u \end{Bmatrix}, \quad (7)$$

$$D_7 = \begin{Bmatrix} (1 + \delta)u & 0 & 0 \\ 0 & (1 - \delta)u & 0 \\ 0 & 0 & u \end{Bmatrix}, \quad (8)$$

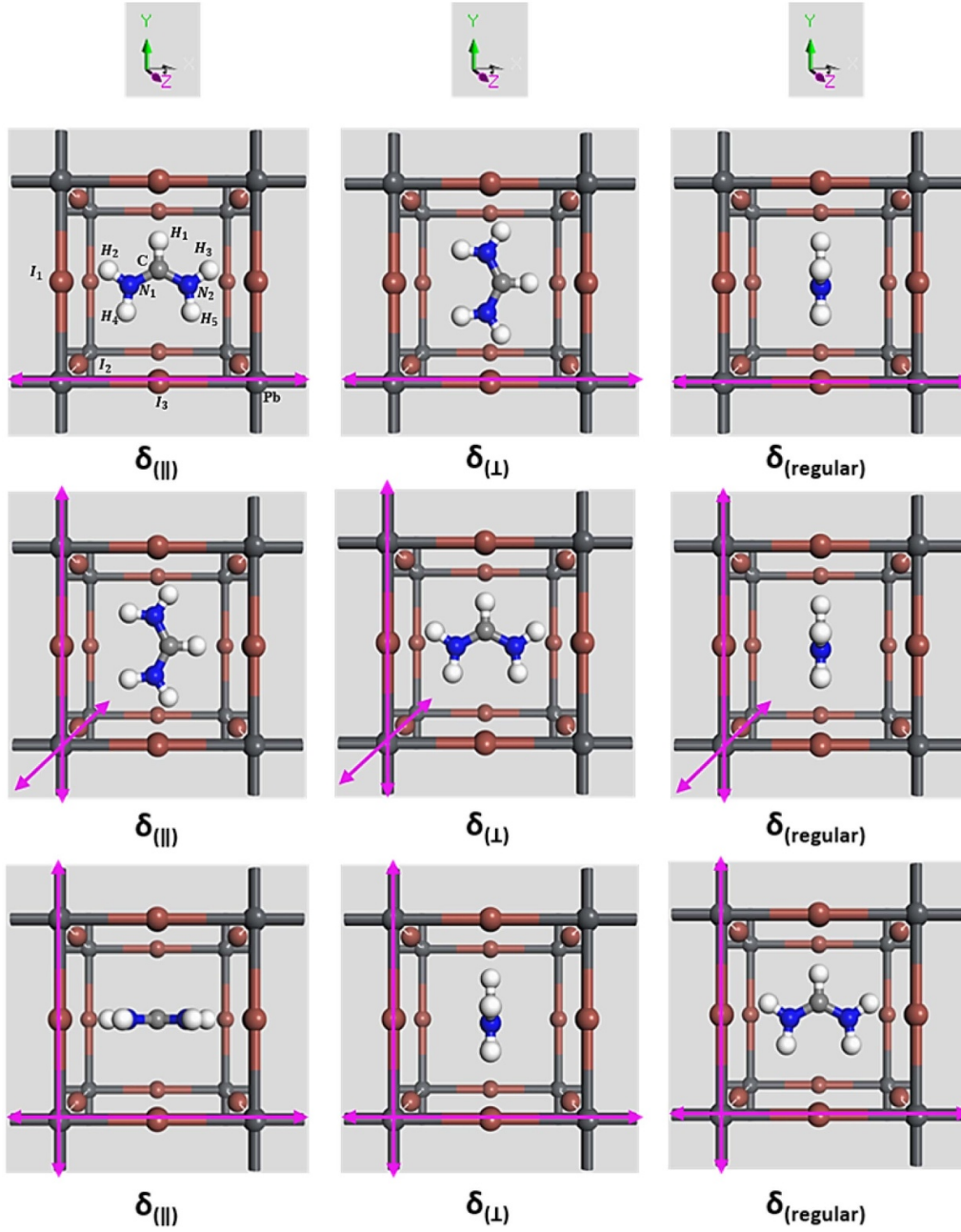


Figure 1. General representation of the orthorhombic strain tensors. The top three show the uniaxial (from left to right: D_1, D_2, D_3) and planar (middle from left to right: D_4, D_5, D_6) bottom from left to right: D_7, D_8, D_9). The top three figures indicate uniaxial - δ_{\parallel} , uniaxial - δ_{\perp} , uniaxial - δ_{regular} , from left to right, respectively. Both middle and bottom rows of the figure are referred to planar - δ_{\parallel} , planar - δ_{\perp} , planar - δ_{regular} deformations, respectively.

$$D_8 = \begin{Bmatrix} (1 + \delta)u & 0 & 0 \\ 0 & u & 0 \\ 0 & 0 & (1 - \delta)u \end{Bmatrix}, \quad (9)$$

$$D_9 = \begin{Bmatrix} u & 0 & 0 \\ 0 & (1 + \delta)u & 0 \\ 0 & 0 & (1 - \delta)u \end{Bmatrix}, \quad (10)$$

where the u is a parameter defined as:

$$u = \frac{1}{(1 - \delta^2)^{\frac{1}{2}}} \quad (11)$$

The strained structures were generated by either just the positive δ_i steps for the symmetric deformations (D_4, D_5, D_6) or both positive and negative for asymmetric ones ($D_1, D_2, D_3, D_7, D_8, D_9$), within the strain amplitudes. Each of the energy difference values represent the total energy subtraction of one strained state, defined by δ_i , from the optimized ground state at $\delta_i = 0$ ($\Delta E_i = E_i(V, \delta) - E(V_0, 0)$). The

calculations of such strained states were performed initially from the converged ground state, modifying the real lattice matrix to the nearest strain step, following the latter procedure to the immediate subsequent deformation, until the strain amplitude is reached (δ_{\max}). With each δ_i step representing a geometrical relaxation, in which the base vectors are optimized under the BFGS algorithm, meanwhile, the strained lattice parameters are kept fixed.

The total energy difference of the nine strain paths ($E_1, E_2, E_3, E_4, E_5, E_6, E_7, E_8, E_9$), are written in terms of a Taylor expansion [24, 25] as:

$$\Delta E_1 = v_0 \left(\tau_1 \delta + \frac{C_{11}}{2} \delta^2 \right), \quad (12)$$

$$\Delta E_2 = v_0 \left(\tau_2 \delta + \frac{C_{22}}{2} \delta^2 \right), \quad (13)$$

$$\Delta E_3 = v_0 \left(\tau_3 \delta + \frac{C_{33}}{2} \delta^2 \right), \quad (14)$$

$$\Delta E_4 = v_0 (2\tau_4 \delta + 2C_{44} \delta^2), \quad (15)$$

$$\Delta E_5 = v_0 (2\tau_5 \delta + 2C_{55} \delta^2), \quad (16)$$

$$\Delta E_6 = v_0 (2\tau_6 \delta + 2C_{66} \delta^2), \quad (17)$$

$$\Delta E_7 = v_0 \left((\tau_1 - \tau_2) \delta + \frac{C_{11} + C_{22} - 2C_{12}}{2} \delta^2 \right), \quad (18)$$

$$\Delta E_8 = v_0 \left((\tau_1 - \tau_3) \delta + \frac{C_{11} + C_{33} - 2C_{13}}{2} \delta^2 \right), \quad (19)$$

$$\Delta E_9 = v_0 \left((\tau_2 - \tau_3) \delta + \frac{C_{22} + C_{33} - 2C_{23}}{2} \delta^2 \right), \quad (20)$$

where the second order coefficient represent the EC values for each strain tensor. The dispersed points from ΔE_i were fitted by a third order polynomial to finally obtain such elastic moduli.

The structural stability from all 12 models is determined by the set of the adiabatic EC values as [26]:

$$\begin{aligned} C_{11} &> 0, \\ C_{11}C_{22} &> C_{12}^2, \\ C_{44} &> 0, \\ C_{55} &> 0, \\ C_{66} &> 0, \end{aligned}$$

$$C_{11}C_{22}C_{33} + 2C_{12}C_{13}C_{23} - C_{11}C_{23}^2 - C_{22}C_{13}^2 - C_{33}C_{12}^2 > 0. \quad (21)$$

At last, the standard error (SE) was determined by the calculation of the statistical deviation from the number of considered deformation steps as:

$$\sigma_x = \frac{\sigma}{\sqrt{n}}. \quad (22)$$

where σ_x is the standard error, σ is the standard population deviation and \sqrt{n} is the square root from the number of deformation steps. Here, the standard deviation is equivalent to the square root of the variance.

4. Results and discussion

As shown in figure 1, it is possible to separate the strain tensors for an orthorhombic structure into two categories. The first three applied strains (D_1, D_2, D_3), are called uniaxial since the deformations act along any of the coordinate axis D_1 for x axis [100], D_2 for y axis [010] and D_3 for z axis [001]. Meanwhile the remaining set of strains ($D_4, D_5, D_6, D_7, D_8, D_9$), are referred as planar, since two different lattice deformations consolidate a modified crystalline plane in the following manner: D_4 and D_9 for YZ plane (100), D_5 and D_8 for XZ plane (010) and finally D_6 and D_7 for XY planes (001).

For the set of uniaxial deformations, whether the normal vector of the cation plane appears to be parallel to the applied strain, it will be defined as regular behavior (δ_{regular}). Meanwhile, when the deformation is applied in a perpendicular direction with respect to the plane of the organic cation, two different tendencies are seen. In one of them, the strain will be parallel to the N–N axis of the FA cation (δ_{\parallel}), and for the second one, the strain tensor modifies the lattice parameters perpendicular to the former axis (δ_{\perp}). For the set of planar deformations, if the applied strain acts on the same plane of the FA cation, it is called regular (δ_{regular}), meanwhile, if any of the applied deformation components are parallel to the N–N axis, they are denoted as δ_{\parallel} , for the immediate next case, if one of the strain components appears to be perpendicular to N–N it will be designated as δ_{\perp} .

The uniaxial - δ_{regular} behavior is obtained for the following combinations of strain paths and FA planes: D_1 [YZ], D_2 [XZ] and D_3 [XY]. On the other hand, the planar - δ_{regular} behavior is shown for: D_4 [YZ], D_5 in [XZ], D_6 [XY], and D_7 [XY], D_8 [XZ] and D_9 [YZ]. For all the cases both ΔE_i vs δ_i plots and their corresponding EC values are independent with respect to the FA clockwise orientation. The respective planes and orientations of the FA cation within the inorganic cage for the uniaxial - δ_{\parallel} cases were obtained for: D_1 [XY 12:00], D_2 [YZ 03:00] and D_3 [XZ 03:00]. Meanwhile, the planar - δ_{\parallel} elastic responses were seen for: D_4 [XY 03:00], D_5 [XY 12:00], D_6 [YZ 03:00], D_7 [XZ 12:00], D_8 [YZ 12:00] and D_9 [XZ 03:00]. Finally, the uniaxial - δ_{\perp} mode occurred for: D_1 in [XY 03:00], D_2 in [YZ 12:00] and D_3 in [XZ 12:00]. With planar - δ_{\perp} obtained for: D_4 [XY 12:00], D_5 [XY 03:00], D_6 [YZ 12:00], D_7 [XZ 03:00], D_8 [YZ 03:00] and D_9 [XZ 12:00], following the notation [plane, orientation].

4.1. Strain amplitude equal to 0.02

The Mulliken charge (MC) population analysis for the uniaxial - δ_{regular} at $\delta_i = -\delta_{\text{max}}$ shows a high bond population in the order of $-0.11e$, with a bond length around 2.83 \AA , both values found among $\text{H}_5 - \text{I}_2$ & $\text{H}_4 - \text{I}_2$ bonds. Meanwhile, a much smaller population is obtained in between $\text{H}_3 - \text{I}_2$ & $\text{H}_2 - \text{I}_2$ bonds ($-0.04 e$ & 2.90 \AA), which is similar to the charge distribution found at the FAPbI_3 ground state [16]. At the opposite strain boundary $\delta_i = \delta_{\text{max}}$, the MC bond population shows similar results as the former case ($-0.11e$ for both $\text{H}_5 - \text{I}_2$ & $\text{H}_4 - \text{I}_2$ and $-0.02e$ for both $\text{H}_3 - \text{I}_2$ & $\text{H}_2 - \text{I}_2$), however, a slight exchange in the bond length is observed, since the values are now distributed as: 2.87 and 2.84 \AA , for both $\text{H}_5 - \text{I}_2$ & $\text{H}_4 - \text{I}_2$ and $\text{H}_3 - \text{I}_2$ & $\text{H}_2 - \text{I}_2$, respectively. Considering the MC of the rest of the deformation steps from all the uniaxial - δ_{regular} results, it is possible to generalize, that the H_4H_5 atoms share a stronger charge distribution in between those halogens situated along a lattice axis perpendicular to the plane of the cation, in comparison with the remaining N–H terminations, i.e. the H_2H_3 atoms. Even more, for all these three cases the applied strain tensors (D_1, D_2, D_3) act along a crystalline direction that do not affect the cation plane, consolidating a uniform elastic behavior, as in the following discussion. At the strain state boundary ($\delta_i = \pm\delta_{\text{max}}$) from both δ_{\parallel} and δ_{\perp} uniaxial cases, the MC analysis shows a different scenario, since the only significant charge distribution occurs just in between $\text{H}_4 - \text{I}_2$ & $\text{H}_5 - \text{I}_2$. For all FA planes, the uniaxial - δ_{\parallel} case shows that the bond population is around $-0.10 e$ with an increased bond length of 2.95 \AA . Compared to a slightly lower set of results for the uniaxial - δ_{\perp} case ($-0.09 e$ and 2.94 \AA), however, both H_2 and H_3 atoms does not have any bond charge contribution in between either of the iodine atoms, which may be explained due to the presence of a modified distance, as complemented by the EDD analysis (see figure 2).

Regarding the ΔE_i vs δ_i plots, it is clear, that there is strong difference between each strain schemes, the set of uniaxial strains (see figure 3 (a) to (c)) show that it is actually possible to achieve lower energy states as δ_i tends to the positive strain boundary (δ_{max}), i.e. a possible minimum energy without the geometry from the unstrained state. For each uniaxial - δ_{regular} , uniaxial - δ_{\parallel} and uniaxial - δ_{\perp} plots, the minimum energy occurs approximately at: $\delta_{\text{regular}}^{\text{min}} = 0.015$, $\delta_{\parallel}^{\text{min}} = 0.019$ and $\delta_{\perp}^{\text{min}} = 0.009$, respectively, generating the following $\frac{b}{a}$ and $\frac{c}{a}$ lattice ratios: 0.967 & 0.993 , 1.028 & 0.982 and 1.078 & 1.008 , respectively, which may stay within the agreement of a pseudo-cubic structure (ground state ratios $\frac{b}{a} = 0.982$, $\frac{c}{a} = 1.008$). The uniaxial EC values (c_{11}, c_{22}, c_{33}) exhibit in general three different tendencies as a function of the FA orientation (see figures 3(d) to (f)). The higher uniaxial c_{ii} value (approximately 48 GPa) is always generated when a perpendicular strain with respect to the FA N–N axis is applied, i.e. a uniaxial - δ_{\perp} , since for all the latter cases the strain path tends to alter the main electronic distribution among the FA cation and the inorganic sub-lattice ($\text{H}_4 - \text{I}_2$ & $\text{H}_5 - \text{I}_2$). The second case appears around 8 GPa below, and such intermediate EC values are likewise a result of a certain combination of both strains and FA orientations,

that modify the structure in a parallel direction to N–N axis (uniaxial - δ_{\parallel}), which is related to the spatial deformation of the charge distribution among the N–H termination from the FA cation and the halogens. On the other hand, it is found that the lowest elastic stiffness response from the three uniaxial deformations is generated by the δ_{regular} case, with a value around 32 GPa , consistently with a deformation that yield the material with relative ease, since the FA cation plane is not modified.

The EC values determined from the set of planar deformations: D_4 to D_6 , are generated out of symmetrical ΔE_i vs δ_i plots around the unstrained state (see figures 4(a) to (c)), i.e. with no energy value exceeding the ground state. In the current description, it is possible to separate them into three different elastic stiffness responses. The EC values that appear to have an independent behavior as a function of the cation orientation (planar - δ_{regular}) possess now the highest magnitude, with a value approximately equal to 1.7 GPa , this upper limit is a result of both strain tensors components applied over the FA plane, i.e. the structure is modified with a fraction of planar - δ_{\parallel} and planar - δ_{\perp} simultaneously. As for the case of the uniaxial elastic response, this higher value is related to a direct modification of the charge distribution among all hydrogen terminations and perpendicular halogens to the FA cation plane. Estimated unbalance population and bond length values were $-0.11e$, 2.91139 \AA ; $-0.12e$, 2.73227 \AA ; $-0.03e$, 2.83458 \AA and $-0.03 e$, 2.97583 \AA , for $\text{H}_4 - \text{I}_2$, $\text{H}_5 - \text{I}_2$, $\text{H}_2 - \text{I}_2$ and $\text{H}_3 - \text{I}_2$, respectively (also further discussed in table 4). Approximately, 0.4 and 0.7 GPa below, appear both planar - δ_{\parallel} and planar - δ_{\perp} , for the intermediate and low-est limit, respectively (figures 4(d) to (f)).

For the remaining EC set of values (c_{12}, c_{13}, c_{23}) calculated by means of planar deformations (figures 5(a) to (c)), it is not possible to directly correlate their magnitudes with the orientation of the FA cation, since the second-order coefficient is linearly combined with another two uniaxial EC constants, as shown in the equations (18) to (20). Therefore, it is expected that the result will be related with the behavior obtained for their respective uniaxial c_{ii} components. For instance, the planar - δ_{regular} is now found for orientations over the FA plane that show a combination of either uniaxial - δ_{\perp} or uniaxial - δ_{\parallel} c_{ii} magnitudes, as for the values of c_{12} over the $[XY]$ plane, since neither c_{11} or c_{22} possess a regular behavior, which is an equivalent case observed over both $[XZ]$ and $[YZ]$ planes for c_{13} and c_{23} EC values, respectively. The latter effect may arise due to a certain compensation among the strain components, that finally generates a non-varying elastic stiffness response in the planar c_{ij} values (8 GPa for both c_{12} and c_{23} and to 12 GPa for c_{13}), shown in figures 5(d) to (f). For the rest of the cases, it is possible to recognize that only one of the uniaxial components from the linear combination needs to possess a δ_{regular} behavior, so that the planar c_{ij} magnitude could show variations following the change in the FA cation orientation.

The numerical EC values show that both uniaxial - δ_{regular} and planar - δ_{regular} behaviors are attained at: c_{33}, c_{66} , and c_{12} , each of them with averages around 32.77 , 1.78 , and 8.09 GPa , for the $[XY]$ FA cation plane, respectively. On the other hand,

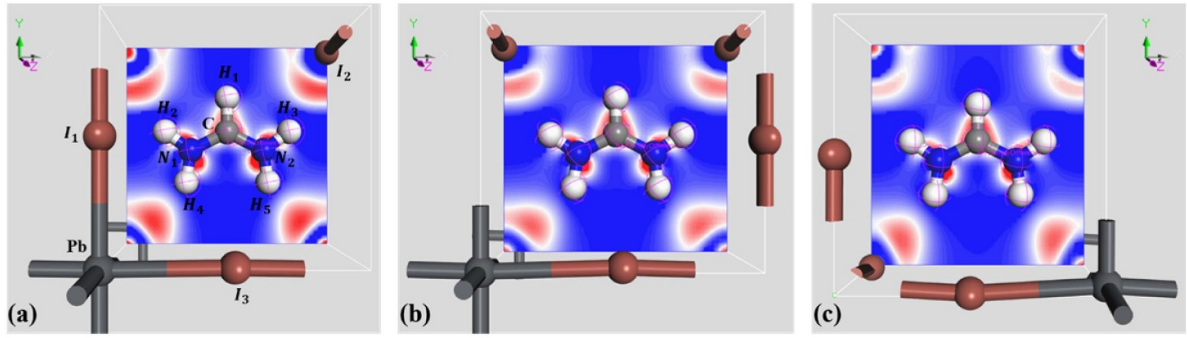


Figure 2. Electron density difference (EDD) of a strained lattice generated at the boundary of a uniaxial deformation (uniaxial - δ_{regular} , uniaxial - δ_{\parallel} and uniaxial - δ_{\perp} , from left to right). Blue-White-Red spectrum displays the electron lack to enrichment, showing a marked diminish of the charge distribution among $H_3 - I_2$ & $H_2 - I_2$, for both uniaxial - δ_{\parallel} and uniaxial - δ_{\perp} , with respect to the uniaxial - δ_{regular} .

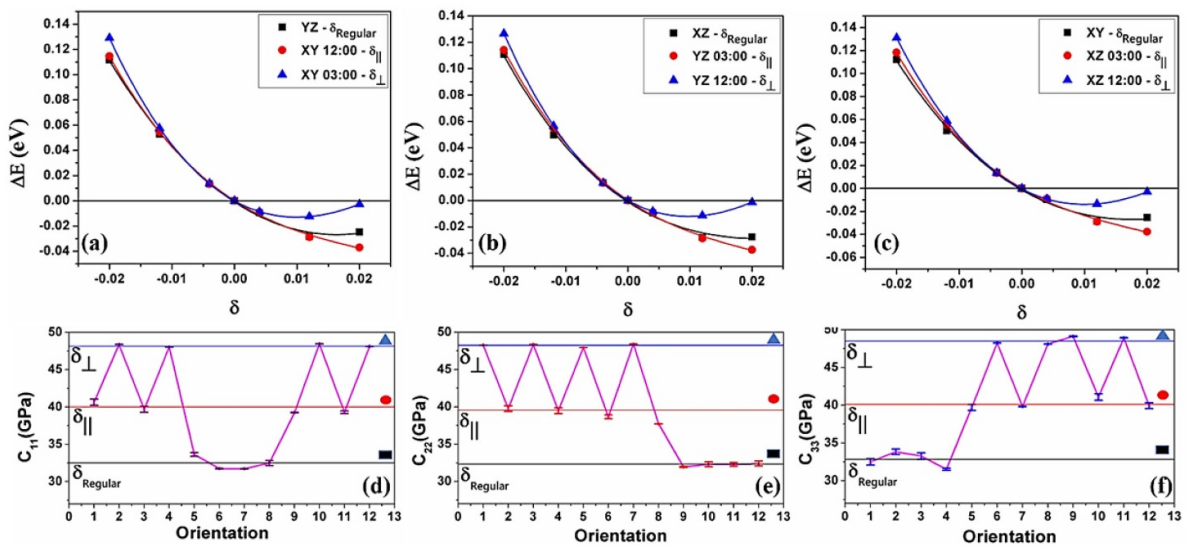


Figure 3. The figures displayed from (a) to (c) show the ΔE_i vs δ_i plots along with their respective EC values, from (d) to (f), determined within the strain amplitude $\delta_{\text{max}} < 0.02$. The associated c_{11} , c_{22} , and c_{33} , values show a fluctuating behavior, among three possible elastic responses, as a result of a combination of the FA orientation and the uniaxial deformation case (uniaxial - δ_{regular} , uniaxial - δ_{\parallel} and uniaxial - δ_{\perp}). The first four points of the orientation-axis displayed from (d) to (f) correspond to the [XY] FA plane alignment, meanwhile, the remaining two sets of four points hold for both [YZ] and [XZ] FA planes, respectively, all of them following the order: 12:00 to 9:00, in clockwise FA alignments. The calculated uncertainty from every c_{ij} value is depicted by error bars centered at each point and the shape symbol, of the possible results, correspond to the respective ΔE_i vs δ_i plots from which it is determined.

for non-regular cases, there is an equivalence in the elastic response in between the FA clockwise orientation at 12:00 and 06:00, which is also present at 03:00 and 09:00, for all c_{ij} values, as it was discussed for the optimized lattice parameters (table 1 [16]). It is prominent to mention that all deformations below an amplitude equal to 0.02 generate positive elastic constants fulfilling the stability criteria for orthorhombic structures (table 1).

The difference in between the set of conditions that determine the stability of two crystal symmetries, i.e. cubic and orthorhombic, turns the comparison of their own EC values nontrivial. On the one hand, both uniaxial c_{ij} set and the planar c_{12} are found to be overestimated with respect to the previous results [10]. As it was shown in equations (2)–(10), none of the strain tensors used for an orthorhombic structure follows both the isotropic deformation and the tetragonal (or the equivalent

orthorhombic) strain tensor used to determine both c_{11} and c_{12} in cubic structures. On the other hand, despite the fact that the set of strain deformations used to obtain c_{44} , c_{55} , and c_{66} , c_{44} , possess a marked resemblance to the symmetric monoclinic tensor, used to determine c_{44} for cubic symmetries [23], the c_{44} , c_{55} , and c_{66} results are underestimated with respect to both the experimentally measured and the calculated cubic EC values, therefore, a direct comparison of the elastic properties among cubic and pseudo-cubic crystalline models is outside the scope of the present paper.

As for the latter case, both bulk (B) and shear (G) moduli, calculated by the Hill-Reuss-Voigt equations [25], possess variations with respect to the cubic-symmetry results (table 2). On the one hand, the low B value found experimentally for FAPbI_3 (from 0.00 to 2.24 GPa) is a consequence of a negative c_{12} [10], which is not seen in the current result

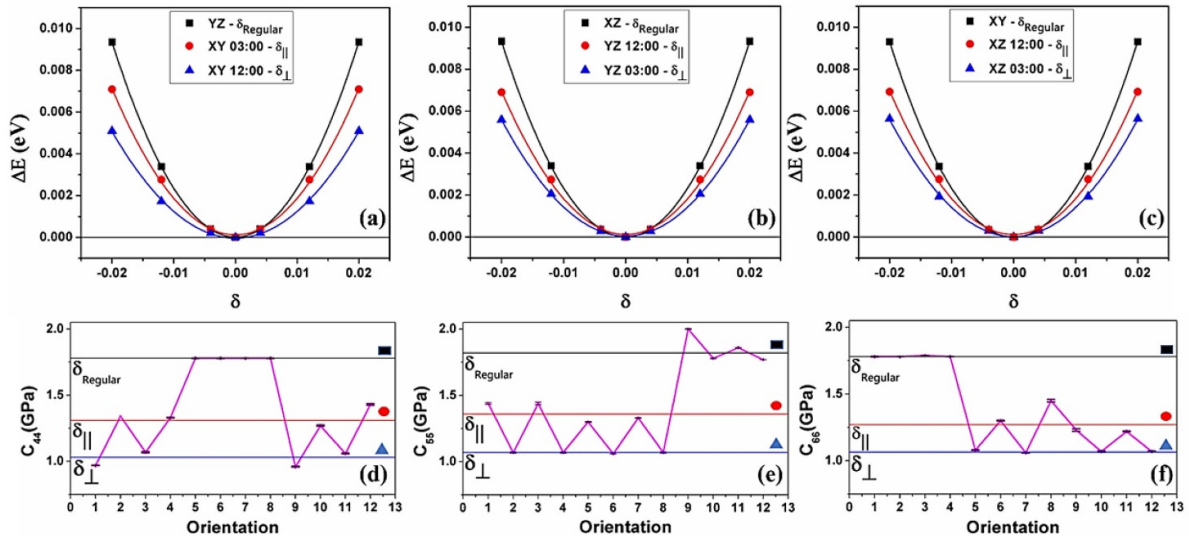


Figure 4. (a)–(c) show the ΔE_i vs δ_i plots along with their respective EC values, from (d) to (f), determined within the strain amplitude $\delta_{\max} < 0.02$. The associated c_{44} , c_{55} , and c_{66} , values show a fluctuating behavior, among three possible elastic responses, as a result of a combination of the FA orientation and the planar deformation case (planar - δ_{regular} planar - δ_{\parallel} , planar - δ_{\perp}). The first four points of the orientation-axis (displayed from (d) to (f)) corresponds to the [XY] FA plane alignment, meanwhile, the remaining two sets of four points hold for both [YZ] and [XZ] FA planes, respectively, all of them following the order: 12:00 to 9:00, in clockwise FA alignments. The calculated uncertainty from every c_{ii} value is depicted by error bars centered at each point and the shape symbol, of the possible results, correspond to the respective ΔE_i vs δ_i plots from which it is determined.

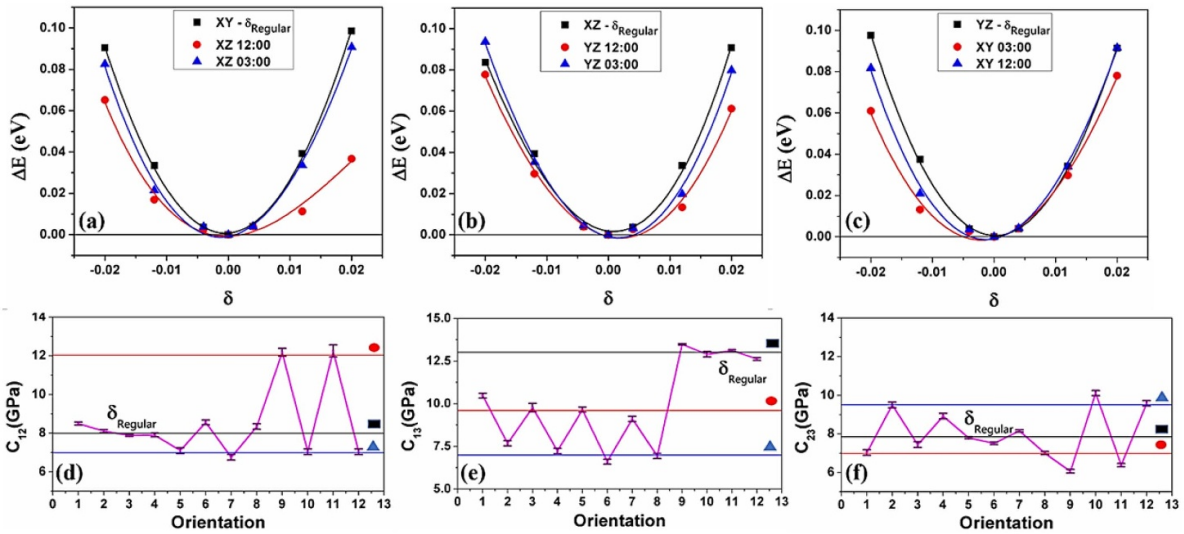


Figure 5. The figures displayed from (a) to (c) show the ΔE_i vs δ_i plots along with their respective EC values, from (d) to (f), determined within the strain amplitude $\delta_{\max} < 0.02$. The associated c_{12} , c_{13} , and c_{23} , values show a fluctuating behavior, among three possible elastic responses, as a result of a combination of the FA orientation and the planar deformation case (planar - δ_{regular} planar - δ_{\parallel} , planar - δ_{\perp}). The first four points of the orientation-axis displayed from (d) to (f)) correspond to the [XY] FA plane alignment, meanwhile, the remaining two sets of four points hold for both [YZ] and [XZ] FA planes, respectively, all of them following the order: 12:00 to 9:00, in clockwise FA alignments. The calculated uncertainty from every c_{ii} value is depicted by error bars centered at each point and the shape symbol, of the possible results, correspond to the respective ΔE_i vs δ_i plots from which it is determined.

(table 1), however, this could be a shred of evidence related to a threshold towards the structural instability, since the cubic second criteria ($c_{11} + 2c_{12} > 0$) will be equal to $0.1 > 0.0$, and as the following discussion shows, the negative EC values are in here found for planar c_{ii} cases. Even though a good agreement could be found among the calculated cubic FAPbI₃ bulk modulus [12, 27] and the [XY 12:00] ground

state, with a latter value equal to 11.79 GPa, obtained following the current calculation scheme, fitting the equation of state to a set of isotropic deformations [23]. Finally, the shear modulus G considered for $\delta_{\max} < 0.02$ show closer values since the Hill–Reuss–Voigt G equations include all planar c_{ii} , supporting the accuracy of the present set of models (table 2).

Table 1. Orthorhombic EC values calculated for the clockwise configurations of the [XY] FA cation structure, including the propagated uncertainty. The present $\delta_{\max} < 0.02$ results are in good agreement with pseudo-cubic EC values determined by first-principles calculations, based on DFT + vdW-DF2 [27], and two sets of cubic EC values experimentally measured by INS [10] and a theoretically determined by a DFT + vdW-TS scheme [12].

	c_{11} [GPa]	c_{22} [GPa]	c_{33} [GPa]	c_{44} [GPa]	c_{55} [GPa]	c_{66} [GPa]	c_{12} [GPa]	c_{13} [GPa]	c_{23} [GPa]
[XY] 12:00	40.63 ± 0.4	48.26 ± 0.0	32.48 ± 0.4	0.97 ± 0.0	1.44 ± 0.0	1.78 ± 0.0	8.49 ± 0.2	10.48 ± 0.5	07.03 ± 0.1
[XY] 03:00	48.38 ± 0.0	39.76 ± 0.3	33.83 ± 0.3	1.34 ± 0.0	1.07 ± 0.0	1.78 ± 0.0	8.11 ± 0.2	07.68 ± 0.2	10.05 ± 0.1
[XY] 06:00	39.68 ± 0.4	48.35 ± 0.0	33.27 ± 0.4	1.07 ± 0.0	1.44 ± 0.0	1.79 ± 0.0	7.89 ± 0.2	09.77 ± 0.3	07.44 ± 0.1
[XY] 09:00	48.01 ± 0.0	39.46 ± 0.4	31.52 ± 0.1	1.33 ± 0.0	1.07 ± 0.0	1.78 ± 0.0	7.90 ± 0.2	06.47 ± 0.1	08.92 ± 0.1
[27]	30.15	31.0	29.85	2.03	5.33	2.60	2.99	7.22	4.26
[10]	11.20 ± 2.0			2.70 ± 0.3				-5.50 ± 2.2	
[12]	20.50			12.30				4.80	

Table 2. Calculated bulk (B) and shear (G) moduli determined by the Hill-Reuss-Voigt equations, including the propagated uncertainty from the set of c_{ij} values. For all clockwise orientations of [XY] FA configurations with $\delta_{\max} < 0.02$. The provided comparison is against experimental [10] and ab initio DFT + vdW-TS [12] as well as DFT-vdW-DF2 [27] results.

	B [GPa]	G [GPa]
[XY]12:00	10.26 ± 0.172	4.90 ± 0.009
[XY]03:00	10.28 ± 0.124	4.90 ± 0.009
[XY]06:00	10.15 ± 0.147	4.95 ± 0.002
[XY]09:00	09.77 ± 0.101	5.02 ± 0.000
[27]	13.25	5.59
[10]	00.00 ± 2.240	8.35 ± 0.100
[12]	15.3	3.6

4.2. Strain amplitude equal to 0.04

If the strain amplitude δ_{\max} is increased beyond 0.02, it is found that the elastic components: c_{44} , c_{55} and c_{66} tend to become a negative value (table 3), making the structure unstable. In specific, FA configurations that involved planar - δ_{\parallel} strains tend to fail the accomplishment of the third, fourth, or fifth orthorhombic stability conditions, respectively (equation (21)). This result is generated by the ΔE_i vs δ_i negative curvatures, reaching strained structures that appear below the ground state energy at $\delta_{\max} = 0.04$ (figure 6(b)), along with a significant change in the SE up to a ± 0.3 GPa, for all the negative cases. However, it does not represent a strong change in the dispersion of points as compared to the negative cases (SE = ± 2.0 GPa), previously reported [10]. Although, the later observation significantly modifies the dispersion generating nonnegligible mismatches during the fitting procedure, this does not change the nonfulfillment of the stability criteria, specifically for c_{44} , c_{55} , and c_{66} (equation (21)), due to the appearance of negative deformation energy values. For both planar - δ_{\perp} and planar - δ_{regular} cases, no changes in their curvature's signs were seen at $\delta_{\max} = 0.04$, however, the point dispersion of the strained states also shows an increased difference associated with each planar c_{ii} value up to $\pm 1 \times 10^{-2}$ GPa.

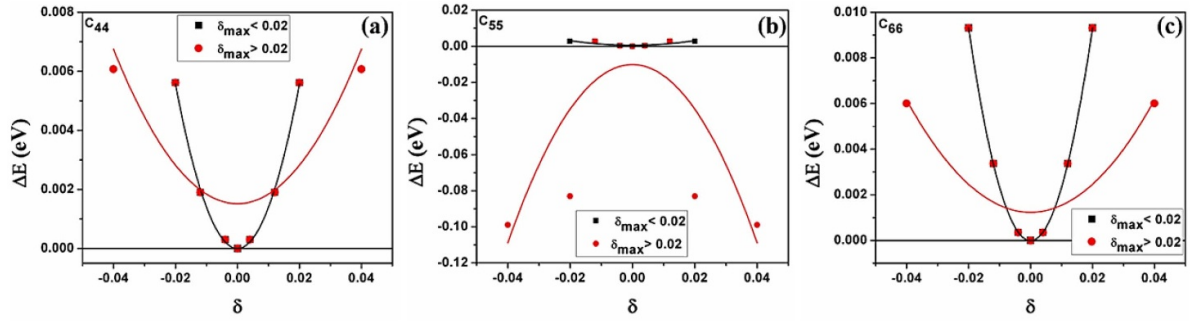
As it was discussed, the MC analysis of the strains below 0.02 show that the chemical bonds among H_4H_5 and H_2H_3 and the iodine atom have both similar distances and populations,

except for the planar - δ_{regular} case (table 4), which means that the system shares in a balanced way the charge distribution among the FA cation and the inorganic unit cell. However, at the extended boundary $\delta_{\max} > 0.02$ under planar - δ_{\perp} strains, the lowest obtained EC values (c_{44}) show an increased distance in between $H_i - I_2$ (where $i = 4, 5$) atoms, meanwhile, the $H_i - I_2$ (where $i = 2, 3$) length decreases, along with a slight reduction of the bond populations. Under the same strain conditions, the bonding distribution of c_{55} (planar - δ_{\parallel}) mainly changes from $H_2 - I_2 \& H_3 - I_2$ to $H_2 - I_1 \& H_3 - I_1$ i.e. the smallest bond population exchanges the iodine position, this relevant charge transfer happens in an unbalanced manner, since only the $H_2 - I_1$ bond populations seems to reach the $H_i - I_2$ (where $i = 4, 5$) distribution, meanwhile the main charge distribution among halogens and hydrogen distributions increase its bond length with a reduced population (table 4). This latter effect follows the strong reduction in the total energy value, which is even more significant than the unstrained energy state, and since the charge transfer is in between two different halogen sites, it implies a tilting of the FA cation outside its initial plane, i.e. around the C-H axis (see figure 7(d)). The obtained MC analysis of the elastic module c_{66} , planar - δ_{regular} displays the most prominent bonding population among $H_5 - I_2 \& H_3 - I_2$ since the only chemical bond occurred this time for the same iodine atom only exchanging the hydrogen termination, therefore, the expected modification in the FA position corresponds this time to a rotation around its plane once the internal coordinates are relaxed.

The EDD plots show the spatial charge distribution as an iso-surface generated from the MC population analysis, where the Blue-White-Red spectrum identifies the areas from electronic lack to enrichment (figure 7). As it was discussed, the unstrained state possesses the most relevant charge distribution located among $H_4 - I_2 \& H_5 - I_2$. For any deformation below the 0.02 strain amplitude, at the boundary point cases of all c_{44} , c_{55} , and c_{66} , the relaxation shows that the cation molecule does not move at all, therefore the charge distribution remains unchanged with respect to the unstrained state. Nevertheless, over such a strain amplitude ($\delta_{\max} > 0.02$), c_{44} shows a similar charge distribution, along with a non-negligible tilting of the organic cation (see figure 5(b)), however, as a result of the strong modification of the charge distribution seen for c_{55} , there is an abrupt FA cation tilt around the C - H_1 FA cation axis, which tends to bring both H_2 and I_1 closer

Table 3. Elastic components values of c_{44} , c_{55} , and c_{66} for all clockwise rotations of the [XY] FA configuration, the values are calculated with six deformations steps under the two tested strain amplitudes: $\delta_{\max} = 0.02$ and $\delta_{\max} = 0.04$, with its corresponding standard error.

	δ	c_{44} [GPa]	c_{55} [GPa]	c_{66} [GPa]
[XY] 12:00	$\delta_{\max} = 0.02$	00.97 ± 0.001	01.44 ± 0.006	01.78 ± 0.001
	$\delta_{\max} = 0.04$	01.45 ± 0.034	-20.60 ± 0.402	00.50 ± 0.084
[XY] 03:00	$\delta_{\max} = 0.02$	01.34 ± 0.000	01.07 ± 0.003	01.78 ± 0.000
	$\delta_{\max} = 0.04$	-21.45 ± 0.341	01.41 ± 0.034	00.92 ± 0.079
[XY] 06:00	$\delta_{\max} = 0.02$	01.07 ± 0.003	01.44 ± 0.009	01.79 ± 0.002
	$\delta_{\max} = 0.04$	01.47 ± 0.0345	-21.30 ± 0.337	01.88 ± 0.067
[XY] 09:00	$\delta_{\max} = 0.02$	01.33 ± 0.002	01.07 ± 0.003	01.78 ± 0.000
	$\delta_{\max} = 0.04$	-22.32 ± 0.352	01.45 ± 0.034	01.43 ± 0.035

**Figure 6.** Deformation energies obtained for the strain tensors: D_4 , D_5 and D_6 (from left to right), applied to the ground state of the [XY] FA 12 o'clock, under the strain amplitude $\delta_{\max} = 0.04$. The planar - δ_{\parallel} strain shows only energy points below the ground state maximum, at the strain amplitudes, generating a negative c_{55} value.**Table 4.** The MC analysis at the strained boundaries of the elastic components c_{44} , c_{55} , and c_{66} of the structure [XY] 12'o clock. Both bond population and bond length values at the unstrained are: $-0.12e$, 2.82312 \AA ; $-0.12e$, 2.82313 \AA ; $-0.03e$, 2.90293 \AA , and $-0.03e$, 2.90294 \AA , for $H_4 - I_2$, $H_5 - I_2$, $H_2 - I_2$ and $H_3 - I_2$, respectively.

[XY] 12:00	$\delta_{\max} = 0.02$			$\delta_{\max} = 0.04$		
	Bond	Population (e)	Length (\AA)	Bond	Population (e)	Length (\AA)
C_{44}	$H_4 - I_2$	-0.12	2.82329	$H_4 - I_2$	-0.11	2.87344
	$H_5 - I_2$	-0.12	2.82329	$H_5 - I_2$	-0.11	2.89060
	$H_2 - I_2$	-0.03	2.90345	$H_2 - I_2$	-0.02	2.83386
	$H_3 - I_2$	-0.03	2.90250	$H_3 - I_2$	-0.02	2.84344
C_{55}	$H_4 - I_2$	-0.12	2.82322	$H_4 - I_2$	-0.09	2.96504
	$H_5 - I_2$	-0.12	2.82322	$H_5 - I_2$	-0.09	2.95160
	$H_2 - I_2$	-0.03	2.90297	$H_2 - I_2$	-	-
	$H_3 - I_2$	-0.03	2.90298	$H_3 - I_2$	-	-
	$H_2 - I_1$	-	-	$H_2 - I_1$	-0.08	2.85976
C_{66}	$H_3 - I_1$	-	-	$H_3 - I_1$	-0.08	2.85472
	$H_4 - I_2$	-0.11	2.91139	$H_4 - I_2$	-	-
	$H_5 - I_2$	-0.12	2.73227	$H_5 - I_2$	-0.10	2.74996
	$H_2 - I_2$	-0.03	2.83458	$H_2 - I_2$	-	-
	$H_3 - I_2$	-0.03	2.97583	$H_3 - I_2$	-0.05	2.65178

together (figure 7(c)), and finally, due to the present distribution of charge for c_{66} , the observed tilting occurred around the axis of the FA cation plane (figure 7(d)).

Despite this prominent effect over perovskite structure, the latter elastic modulus is positive, suggesting the possibility of an energetically favored tilting of the FA along its plane axis. These cation relaxation obtained through modifications generated by planar - δ strains are in agreement with the results of S. Kanno, since the authors demonstrated that the rotational

energy barrier of the organic cation in FAPbI₃ is higher around θ , which is an internal coordinate defined by the rotation along and axis penetrating the FA cation by its carbon atom to its center of mass [15], a similar FA cation tilting that is driven by a strain that could turn the whole structure unstable beyond a certain strain amplitude, that may be proved to be also characteristic for the specific halogen atom present in the inorganic cage. The mechanical instability here determined by the numerical value of the elastic constants, followed by both

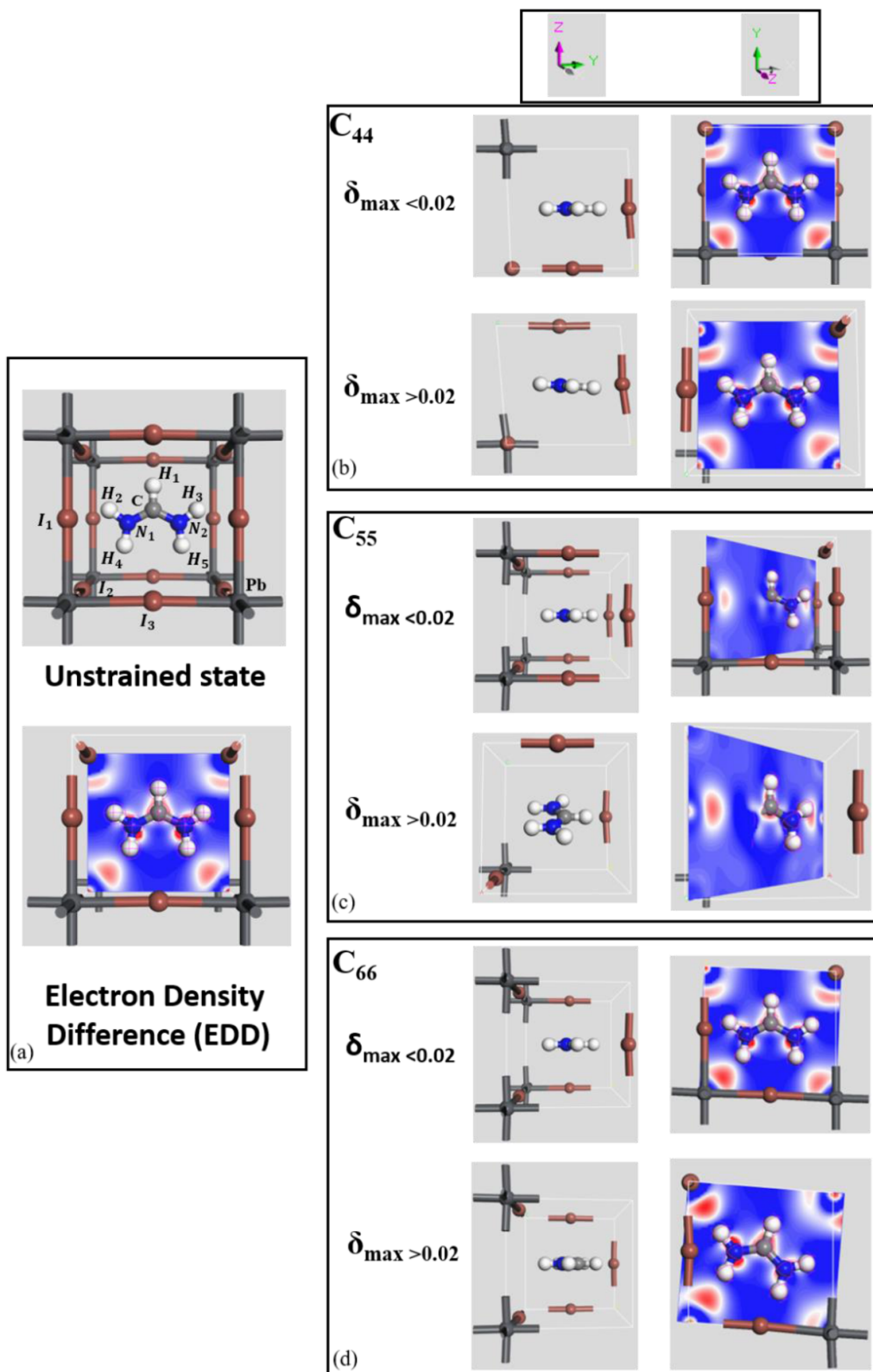


Figure 7. The EDD plots at the strain boundaries for the elastic components: c_{44} , c_{55} , and c_{66} of the [XY] FA 12 o'clock configurations, the results are shown for both $\delta_{\max} < 0.02$ and $\delta_{\max} > 0.02$ strain amplitudes. Blue-White-Red spectrum displays the electron lack to enrichment, showing a marked charge transfer that describes the FA cation tilting, around the C - H₁ axis for the exchange of the iodine position and around the plane axis while transferring the charge among hydrogen terminations, for c_{66} , at the structure instability state, respectively.

the unbalanced electronic population in between hydrogen to halogens and the collective organic cation tilting, could trigger the structural instability that induces the phase transition from black to yellow perovskite [28].

5. Conclusion

The mechanical stability response of FAPbI₃ perovskites structure were investigated and presented based on their organic cation position, using DFT-GGA method through the CASTEP module available in Material studio software. By employing two different strain amplitudes, it was possible to observe a generalized elastic stiffness behavior. First, under a strain amplitude (0.02) limit that generates a set of EC values that fulfill all the stability conditions of pseudo-cubic (orthorhombic) structure, the highest elastic stiffness response is found for uniaxial - δ_{\perp} strains, meanwhile, those deformations with both displacement components acting over the FA cation plane, show the highest planar c_{ii} magnitude, a value which is independent of the FA orientation. The obtained EC values, as well as both Bulk and Shear moduli results, agree with previously reported literatures. Secondly, with an increasing amplitude (0.04) the planar c_{ii} results start to show negative values, that made the structure unstable, specifically for deformations featuring a planar - δ_{\parallel} strain as one of the components. The instability mechanism is described by means of both population and bond length observed among H_i - I₂ (where $i = 2, 3$), which is abruptly modified, outside the stability threshold, which is found in between the strain amplitudes $\delta_{\max} = 0.02$ to 0.04, for pristine FAPbI₃, i.e. once $\delta_{\max} > 0.02$, into a H₂ - I₁ distribution with magnitudes as prominent as H_i - I₂ (where $i = 4, 5$), followed by a tilting of the FA cation around C - H₁, once the atomic position are relaxed. We believe that the present study provides noticeable explanations to understand the instability mechanism of formamidinium based perovskite structures, that could be used to describe the black alpha phase to yellow delta phase transition (which is not suitable for photovoltaic applications), implicating the performance of actual devices.

Acknowledgments

The authors are grateful to the partial support from CONACYT-SENER project No. 263043 and for the computing time granted by LANCAD in the Supercomputer Hybrid Cluster Xiuhcoatl at GENERAL COORDINATION OF INFORMATION AND COMMUNICATIONS TECHNOLOGIES (CGSTIC) of CINVESTAV (URL: <http://clusterhibrido.cinvestav.mx/>). In particular, authors SK and JJR are gratefully to CONACYT for the doctoral and postdoctoral fellowship granted, respectively.


ORCID iDs

S Karthick  <https://orcid.org/0000-0002-0212-2752>

J J Ríos-Ramírez  <https://orcid.org/0000-0003-0761-3937>

S Velumani  <https://orcid.org/0000-0002-0998-7900>

K S Martirosyan  <https://orcid.org/0000-0003-2493-0918>

H Castaneda  <https://orcid.org/0000-0002-9252-7744>

References

- [1] Stoumpos C C, Malliakas C D and Kanatzidis M G Semiconducting tin and lead iodide perovskites with organic cations: phase transitions, high mobilities, and near-infrared photoluminescent properties 2013 *Inorg. Chem.* **52** 9019
- [2] Li D, Meng J, Niu Y, Zhao H and Liang C 2015 Understanding the low loss mechanism of general organic-inorganic perovskites from first-principles calculations *Chem. Phys. Lett.* **627** 13
- [3] Kieslich G, Sun S and Cheetham A K 2015 An extended tolerance factor approach for organic-inorganic perovskites *Chem. Sci.* **6** 3430
- [4] Zhumekenov A A et al Formamidinium lead halide perovskite crystals with unprecedented long carrier dynamics and diffusion length 2016 *ACS Energy Lett.* **1** 32–37
- [5] Davies C L, Borchert J, Xia C Q, Milot R L, Kraus H, Johnston M B and Laura M H Impact of the organic cation on the optoelectronic properties of formamidinium lead triiodide 2018 *J. Phys. Chem. Lett.* **9** 4502
- [6] Han Q et al 2016 Single crystal formamidinium lead iodide (fapbi3): insight into the structural, optical, and electrical properties *Adv. Mater.* **28** 2253
- [7] Yang J et al 2017 Acoustic-optical phonon up-conversion and hot-phonon bottleneck in lead-halide perovskites *Nat. Commun.* **8** 14120
- [8] Eperon G E, Stranks S D, Menelaou C, Johnston M B, Herza L M and Snaith H J 2014 Formamidinium lead trihalide: a broadly tunable perovskite for efficient planar heterojunction solar cells *Energy Environ. Sci.* **7** 982
- [9] Manspeaker C, Venkatesan S, Zakhidov A and Martirosyan K 2017 Role of interface in stability of perovskite solar cells *Curr. Opin. Chem. Eng.* **15** 1
- [10] Ferreira A et al Elastic softness of hybrid lead halide perovskites 2018 *Phys. Rev. Lett.* **121** 085502
- [11] Tkatchenko A and Schefer M Accurate molecular van der waals interactions from ground-state electron density and free-atom reference data 2009 *Phys. Rev. Lett.* **102** 073005
- [12] Wang J F, Fu X N and Wang J T First-principles analysis of the structural, electronic, and elastic properties of cubic organic-inorganic perovskite hc(nh2)2pbi3 2017 *Chin. Phys. B* **26** 106301
- [13] Carignano M A, Saeed Y, Aravindh S A, Roqan I S, Even J and Katan C 2016 A close examination of the structure and dynamics of hc(nh2)2pbi3 by md simulations and group theory *Phys. Chem. Chem. Phys.* **18** 27109
- [14] Lee K, Murray E D, Kong L, Lundqvist B I and Langreth D C 2010 Higher accuracy van der waals density functional *J. Phys. Rev. B* **82** 081101(R)
- [15] Kanno S, Imamura Y and Hada M Theoretical study on rotational controllability of organic cations in organic-inorganic hybrid perovskites: hydrogen bonds and halogen substitution 2017 *J. Phys. Chem. C* **127** 26188
- [16] Karthick S, Rios-Ramirez J and Velumani S 2018 12 possible orientations of organic formamidinium cation and its structural analysis by first-principles calculations using van der waals-density functional theory *15th Int. Conf. on Electrical Engineering Computing Science and Automatic Control (CCE)* (<https://doi.org/10.1109/ICEEE.2018.8533994>)
- [17] Segall M D, Lindan P J D, Probert M J, Pickard C J, Hasnip P J, Clark S J and Payn M C 2002 First-principles simulation: ideas, illustrations, and the castep code *J. Phys.: Condens. Matter.* **14** 2717

- [18] BIOVIA, Dassault systems Materials Studio, Discovery Studio Modeling Environment San Diego: Accelrys Software Inc. 17.2.0. 1626
- [19] Perdew J P, Burke K and Ernzerhof M generalized gradient approximation made simple 1996 *Phys. Rev. Lett.* **77** 3865
- [20] Vanderbilt D Soft self-consistent pseudopotentials in a generalized eigenvalue formalism 1990 *Phys. Rev. B* **41** 7892
- [21] Pfrommer B G, Cote M, Louie S G and Cohen M L Relaxation of crystals with the quasi-newton method 1997 *J. Comput. Phys.* **131** 233
- [22] Weller M T, Weber O J, Frost J M and Walsh A Cubic perovskite structure of block formamidinium lead iodide, [hc(nh₂)₂]₂pbi₃ at 298 k 2015 *J. Phys. Chem. Lett.* **6** 3209
- [23] Vitos L 2007 *Computational Quantum Mechanics for Materials Engineers: The EMTO Method and Applications* (Berlin: Springer)
- [24] Reshak A and Jamal M 2012 Dft calculation for elastic constants of orthorhombic structure within wien2k code: a new package (ortho-elastic) *J. Alloys Compd.* **543** 147
- [25] Ravindran P, Fast L, Korzhavyi P A, Johansson B, Wills J and Eriksson O Density functional theory for calculation of elastic properties of orthorhombic crystals: application to TiSi₂ 1998 *J. Appl. Phys.* **84** 4891
- [26] Mouhat F and Coudert F X Necessary and sufficient elastic stability conditions in various crystal systems 2014 *Phys. Rev. B* **90** 224104
- [27] Lei G, Gang T and Jiawang H 2019 Mechanical properties of formamidinium halide perovskites fabx₃ (fa = ch(nh₂)₂; b = pb, sn; x = br, i) from first-principles *Chin. Phys. Lett.* **36** 056201
- [28] Jiang S, Luan Y, Jang J I, Baikie T, Huang X, Li R, Saouma F O, Wang Z, White T J and Fang J Phase transitions of formamidinium lead iodide perovskite under pressure 2018 *J. Am. Chem. Soc.* **140** 13952–7